

Supporting information to: Facile pentagon formation in the dissociation of polyaromatics

Arjen J. de Haas,[†] Jos Oomens,^{†,¶} and Jordy Bouwman^{*,†,‡}

[†]*Radboud University, Institute for Molecules and Materials, FELIX Laboratory,
Toernooiveld 7c, 6525ED Nijmegen, The Netherlands*

[‡]*Current address: Sackler Laboratory for Astrophysics, Leiden Observatory, Leiden
University, P.O. Box 9513, 2300 RA Leiden, The Netherlands*

[¶]*van 't Hoff Institute for Molecular Sciences, University of Amsterdam, Science Park 904,
1098XH, Amsterdam, The Netherlands*

E-mail: bouwman@strw.leidenuniv.nl

Ion trapping

The experiment is operated at a repetition rate of 10 Hz and the measurement cycle is displayed in Fig. 1. The cycle starts with the ArF laser that generates the ions inside the trap by multiphoton (dissociative) ionization. Next, the SWIFT pulse is applied to the repeller endcap of the ion trap to isolate the fragment of interest. This fragment is subsequently exposed to the mid-IR radiation from FELIX, after which the ion and IR induced fragments are ejected from the trap to record their time-of-flight mass spectra.

The effect of an increase of the trapping time on the ion intensity of the species of interest has been investigated and is shown in Fig. 2. The intensity of the target ion at $m/z = 152$

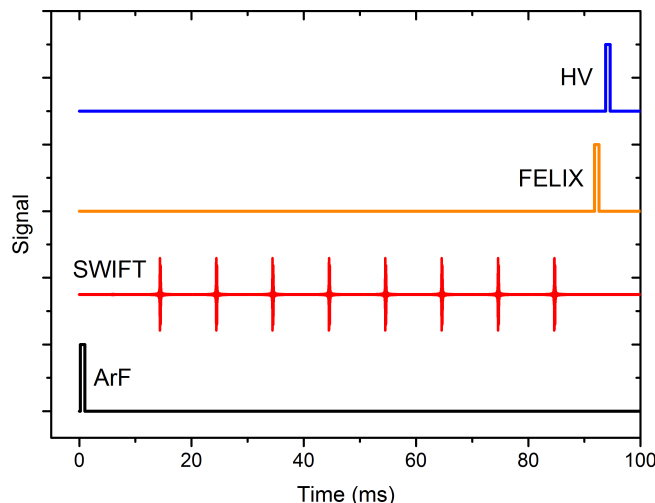


Figure 1: Duty cycle of the experiment displaying the sequence and timing of the UV ionization laser pulse (ArF), the SWIFT mass isolation, the FELIX infrared laser pulse and the high voltage extraction pulse (HV) ejecting the ions from the ion trap into the TOF tube.

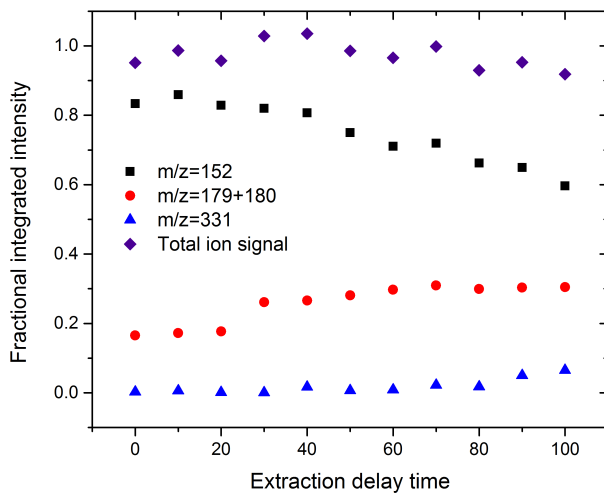


Figure 2: Ion intensities as a function of the delay time between UV dissociative ionization and ion extraction into the TOF MS. At $t = 0$ ms the mass-isolation of the $m/z = 152$ fragment from phenanthridine by SWIFT is complete.

decreases significantly as the trapping time is extended, while at the same time an increase of the mass peaks at $m/z = 179$ and $m/z = 180$ is observed. In addition, a broad mass peak centered around $m/z = 331$ emerges as the trapping time is increased. This peak corresponds to a complex of the isolated $m/z = 152$ ions with a neutral phenanthridine

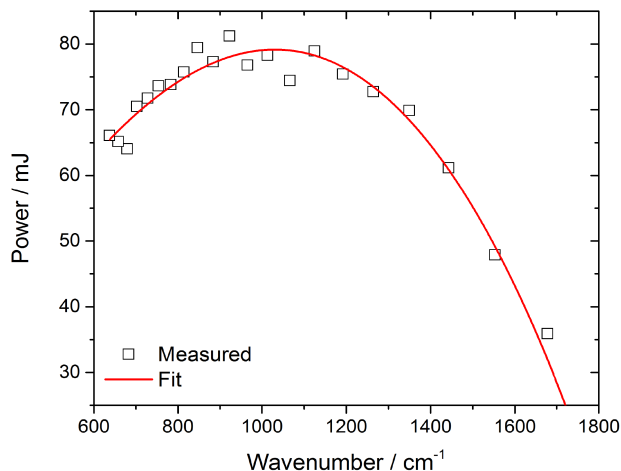


Figure 3: A typical Free Electron Laser power curve that is used for power correction of the IRMPD spectra.

molecule. Given the decay in intensity of our target ion over time, only one FEL pulse was used in the IRMPD spectroscopy experiments of the isolated $m/z = 152$ ions, so that the trapping time was limited to ≤ 100 ms.

FEL power correction

The spectra are corrected for fluctuations in the mid infrared laser pulse energies emitted by the FEL by scaling the IRMPD induced fragment ion intensities to the measured FEL pulse energy. A typical FEL power curve is displayed in Fig. 3. From this figure it can be seen that the FEL power is drops drastically at the high frequency side of the spectrum.

Spectral assignments

Tables 1-4 summarize the computed and measured frequencies for the vibrational modes of $C_{12}H_8$ isomers BPh^+ , $1EN^+$, $2EN^+$ and AcN^+ , respectively. Also shown in these tables are normalized infrared intensities, assignments to the vibrational modes and their corresponding symmetries.

Table 1: Calculated and experimental IRMPD vibrational frequencies of $\text{Ace}^{\cdot+}$. In-plane modes are denoted IP and out-of-plane modes are denoted with OOP.

Calculated (B3LYP/6-311++(2d,p))			Experimental (IRMPD)		
Mode	Description	Wavenumber (cm^{-1})	Intensity	FELIX wavenumber (cm^{-1})	Shift (%)
B ₁	OOP C-H bend	760	0.28	751	-1.18
B ₁ +B ₂	OOP C-H bend + C=C IP stretch	842	0.43	834	-1.00
				949	
B ₂	IP bend/stretch?	1007	0.28	1013	0.6
B ₂	IP bend/stretch?	1073	1	1072	-0.07
B ₂	IP bend/stretch?	1173	0.26	1176	0.26
B ₂	?	1215	0.14	<i>1218</i>	0.25
A ₂	IP C-H bend	1246	0.28	<i>1255</i>	0.72
A ₁	IP C=C bend/stretch?	1297	0.19	<i>1308</i>	0.85
B ₂	IP C-H bend	1337	0.09	1333	-0.30
A ₁	IP	1389	0.14	1391	0.14
A ₁	IP C-H bend	1436	0.04	1436	0.00
A ₁	2 IP C=C?	1478	0.03		
B ₂	2 IP central C=C stretch	1558	0.66	1556	-0.13

Table 2: Calculated and experimental IRMPD vibrational frequencies of $\text{BPh}^{\cdot+}$. In-plane modes are denoted IP and out-of-plane modes are denoted with OOP.

Calculated (B3LYP/6-311++(2d,p))			Experimental (IRMPD)		
Mode	Description	Wavenumber (cm^{-1})	Intensity	FELIX wavenumber (cm^{-1})	Shift (%)
B _{3u}	OOP C-H bend	739	0.57	741	0.27
				834	
B _{1u}	IP ring stretch	956	0.17	964	0.84
B _{2u}	IP C-H bend	1125	0.08	<i>1122</i>	-0.27
B _{1u}	IP C-H bend	1158	0.03	<i>1161</i>	0.26
B _{1u}	IP C-H bend	1286	0.08		
B _{1u}	IP C-H bend	1399	0.04	1392	-0.5
B _{2u}	IP C=C bend	1463	0.06		
B _{1u}	IP C=C stretch/CH bend	1515	1	1494	-1.39

Assignments of HCN-loss products

The IR spectrum of the $[\text{M} - 27]^{\cdot+}$ fragment from acridine (Fig. 4A) shows the best match with the computed spectrum of $\text{BP}^{\cdot+}$ (Fig. 4C) that is overplotted in green onto the acridine fragment spectrum in panel A). While the band at 752 cm^{-1} matches reasonably well with the mode at 742 cm^{-1} in the spectrum of $\text{BPh}^{\cdot+}$ in Fig. 4E, the small mismatch in peak position combined with the absence of the other $\text{BPh}^{\cdot+}$ features around 970 and 1490 cm^{-1} rule out $\text{BPh}^{\cdot+}$ as the product ion structure. Although the positions of the bands at 752 , 1097 and 1343 cm^{-1} in the spectrum of the acridine $[\text{M} - 27]^{\cdot+}$ fragment match reasonably

Table 3: Calculated and experimental IRMPD vibrational frequencies of 1-Eth-Naph⁺. In-plane modes are denoted IP and out-of-plane modes are denoted with OOP.

Calculated (B3LYP/6-311++(2d,p))				Experimental (IRMPD)	
Mode	Description	Wavenumber (cm ⁻¹)	Intensity	FELIX wavenumber (cm ⁻¹)	Shift (%)
A' (2x) +A''	Eth C-H IP + OOP bend	685	0.38	690	0.73
A''	2 OOP C-H bend	751	0.35	747	-0.53
A''	OOP C-H bend	798	0.14	787	-1.38
		-	-	827	-
A'	IP C-H bend	1007	0.09	1010	0.30
A'	IP C-H bend	1106	0.04	1099	-0.63
A' (2x)	IP C-H bend	1161	0.23	1115	-0.18
A' (2x)	2 IP C-H bend	1212	1	1209	-0.25
A'	?	1316	0.63	1335	1.44
A'	IP C=C stretch	1389	0.14	1396	0.50
A'	IP C=C stretch	1432	0.11		
A' (2x)	IP C=C stretch	1518	0.69	1504	-0.92

Table 4: Calculated and experimental IRMPD vibrational frequencies of 2-Eth-Naph⁺. In-plane modes are denoted IP and out-of-plane modes are denoted with OOP.

Calculated (B3LYP/6-311++(2d,p))				Experimental (IRMPD)	
Mode	Description	Wavenumber (cm ⁻¹)	Intensity	FELIX wavenumber (cm ⁻¹)	Shift (%)
A'+A''	Eth- C-H IP + OOP bend	688	0.18	690	0.25
A'' + 2 A'2	OOP C-H bend, 1 C=C stretch	745	0.12	747	0.24
A'	OOP C-H bend	820	0.05	828	0.98
A'	OOP C-H bend	873	0.07	880	0.80
A'	OOP C-H bend	926	0.08	930	0.44
A'	IP C-H bend	1016	0.02	1034	1.77
A'	IP C-H bend	1117	0.21	1115	-0.18
2 A'	2 IP C-H bend	1159	0.06		
A'	IP C-H bend	1203	0.61	1200	-0.25
A'	IP C=C stretch	1334	0.28	1332	-0.15
A'	IP C=C stretch	1379	0.20	1380	0.07
A'	IP C=C stretch	1420	0.11	1418	-0.14
2 A'	2 IP C=C stretch	1507	1	1482	-1.66

well with features in the spectrum of AcN⁺ in Fig. 4D, the relative intensities do not match. Furthermore, other AcN⁺ resonances, specifically the one at 834 cm⁻¹, are not clearly present in the spectrum of the acridine fragment, ruling out this species as a main contributor. The IR spectra of 1EN⁺ and 2EN⁺ (Fig. 4F and G) do not appear to match at all with that of the acridine *m/z* 152 fragment, leaving BP⁺ as the only candidate structure, yet a small contribution of AcN⁺ cannot be excluded entirely. The three main resonances and two weaker transitions observed in the experimental spectrum closely resemble the bands in the computed BP⁺ spectrum. The computed feature at 1560 cm⁻¹ is not observed in the

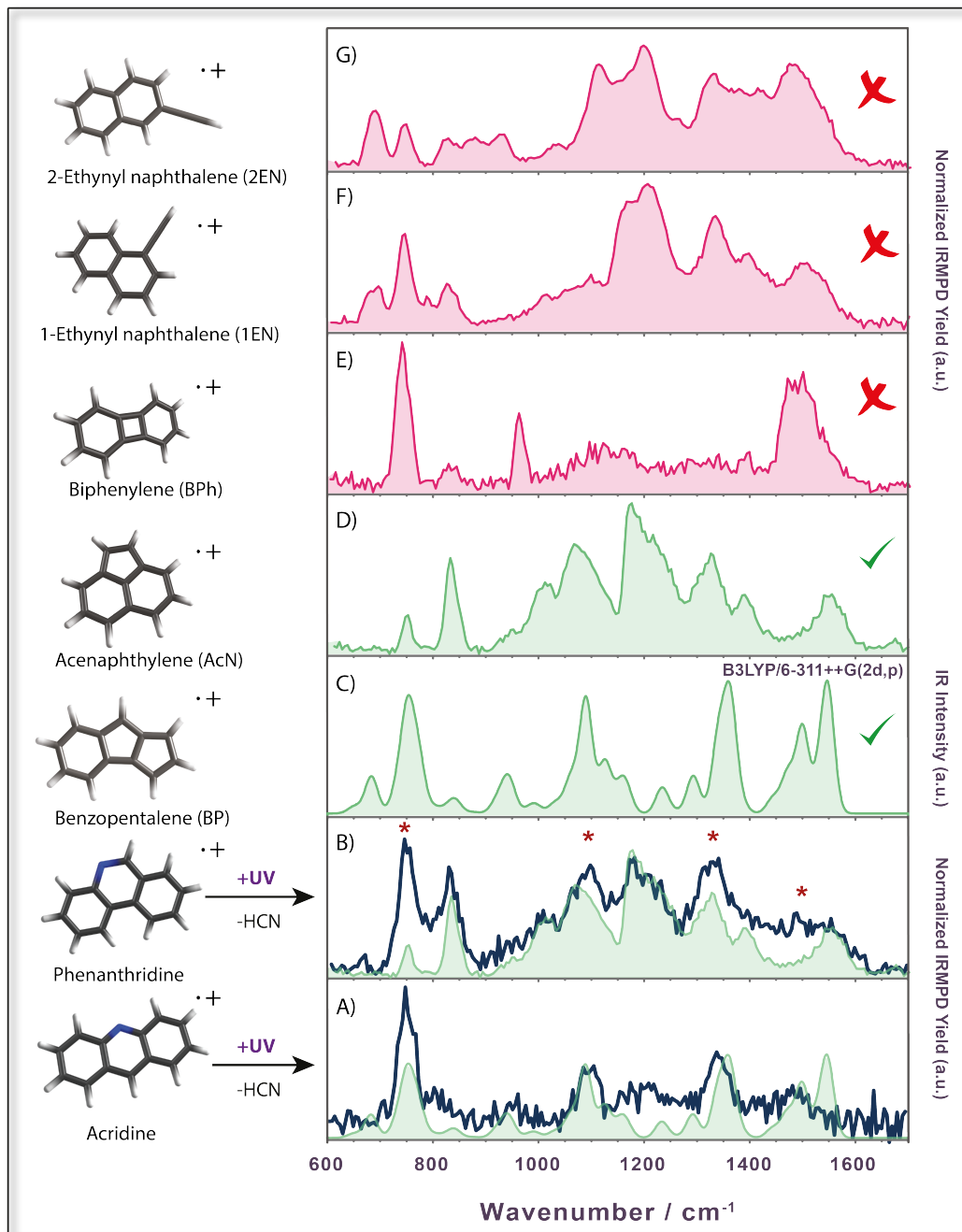


Figure 4: IRMPD spectra of the $[M - 27]^+$ fragments of acridine (A) and phenanthridine (B) at m/z 152, plotted together with the computed IR-spectrum of benzopentalene $^+$ (C) and the measured IRMPD spectra of acenaphthylene $^+$ (D), biphenylene $^+$ (E), 1-ethynyl-naphthalene $^+$ (F), and 2-ethynyl-naphthalene $^+$ (G). The spectrum of benzopentalene $^+$ is overplotted on panel A) to facilitate comparison. Similarly, the spectrum of acenaphthylene $^+$ is overplotted on panel B). The stars (*) in panel B) mark the features of this spectrum that are attributed to benzopentalene $^+$

experimental spectrum, which is likely caused by reduced FEL pulse energies towards the high-frequency end of the spectrum (see Fig. 3).

The spectrum of the $[M - 27]^+$ fragment from phenanthridine shown in Fig. 4B exhibits the same features as the acridine fragment spectrum in panel A (bands marked with a “*”), but is complemented by additional resonances superimposed on a broad absorption stretching from 900 to 1400 cm^{-1} . The presence of all bands that are observed in the spectrum of the acridine fragment suggests that BP^+ is also a primary dissociation product of phenanthridine. The slightly weaker bands at 835 and 1180 cm^{-1} match perfectly with two of the strongest features in the spectrum of AcN^+ shown in Fig. 4D and plotted in green onto the fragment spectrum in Fig. 4B to facilitate the comparison. Close inspection reveals that AcN^+ can also explain the broad structure between 900 and 1400 cm^{-1} . We thus conclude that the dissociative ionization of phenanthridine proceeds along two parallel pathways yielding BP^+ and AcN^+ .

Other products

The IRMPD spectra shown in Fig. 4 (and Fig. 3 and 5 in the main text) are constructed from the H- and H_2 -loss mass channels, which are the only IRMPD induced dissociation channels observed for these species. However, the $m/z = 152$ fragment formed in the dissociative ionization of acridine in panel Fig. 4A exhibits an additional IRMPD channel corresponding to the loss of a neutral fragment of 27 mass units, resulting in an ion at $m/z = 125$. The spectrum obtained when monitoring this IRMPD fragment channel is shown in the top panel of Fig. 5. For comparison, the spectrum resulting from the IRMPD induced H and H_2 -loss channel is shown in the bottom panel of this figure.

The spectra shown in Fig. 5 exhibit clearly distinct spectral features. Those resulting from H- and H_2 -loss are attributed to a $\text{C}_{12}\text{H}_8^+$ species benzopentalene (see main text). The ion signal formed through IRMPD of $m/z = 152$ and detected at $m/z = 125$ can

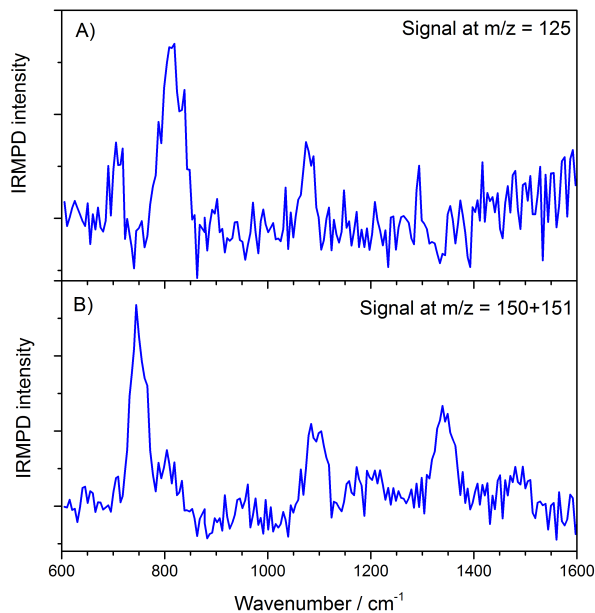


Figure 5: The IRMPD spectra of the $m/z = 152$ fragments resulting from dissociative ionization of acridine (A) recorded by measuring the formation of an IRMPD product at $m/z = 125$ and (B) recorded by measuring the H- and H₂ loss induced by IRMPD.

be attributed to either HCN- or C₂H₃·-loss from the isolated $m/z = 152$ peak. Loss of C₂H₃· by IRMPD requires a two-step process and is deemed unlikely. Furthermore, the observed resonances at 708, 812 and 1080 cm⁻¹ do not match any of the C₁₂H₈^{·+} spectra. This suggests that the spectrum is due to an $m/z=152$ ion that still contains the nitrogen atom and undergoes HCN-loss upon IRMPD. The precursor $m/z=152$ ion must then have been formed by UV induced C₂H₃·-loss from acridine instead of by HCN-loss. Such parallel dissociation pathways have indeed been reported for acridine based on high resolution mass spectrometry.¹ No attempt was made here to assign the structure of this alternative $m/z=152$ species of C₁₁H₆N composition.

C₁₃H₉N^{·+} potential energy surface

Figure 6 shows the computed potential energy surface connecting acridine^{·+} and phenanthridine^{·+}. This mechanism starts from acridine with a hydrogen shift, followed by 6-6 to 5-7

ring conversion. After a second hydrogen shift and 5-7 to 6-6 ring conversion, phenanthridine is reached. The second hydrogen shift with barrier of 4.58 eV constitutes the rate-limiting step for this isomerization pathway.

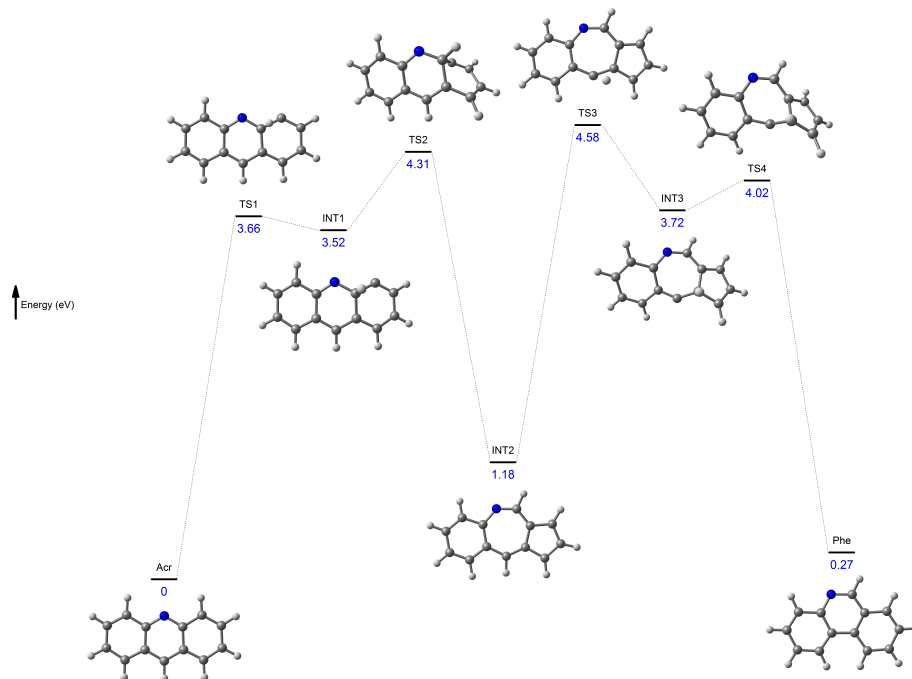


Figure 6: Potential energy surface leading from acridine⁺ to phenanthridine⁺.

The pathway from acridine⁺ to BP⁺ + HCN, as shown in Fig. 7, is initiated by the same hydrogen shift and 6-6 to 5-7 ring conversion as that for the acridine to phenanthridine isomerization. The transition state of the ring conversion (TS2) corresponds to the highest energy barrier for this reaction pathway (4.31 eV). HCN can be lost from the central 7-membered ring rather easily now, resulting in the benzopentalene radical cation.

Phenanthridine⁺ may expel HCN and form BP⁺ via very similar pathway as that of acridine and the path is shown in Fig. 8. Again, a hydrogen shift followed by a 6-6 to 5-7 ring conversion constitute the first two steps of the PES. From the thus formed structure (INT9), HCN can be ejected from the central 7-membered ring leading to the formation of BP⁺. The highest energy barrier for this pathway is the 6-6 to 5-7 ring conversion (TS9) located at an energy of 3.78 eV with respect to phenanthridine⁺.

The pathways connecting phenanthridine⁺ with AcN⁺ and 1EN⁺ proceed through the

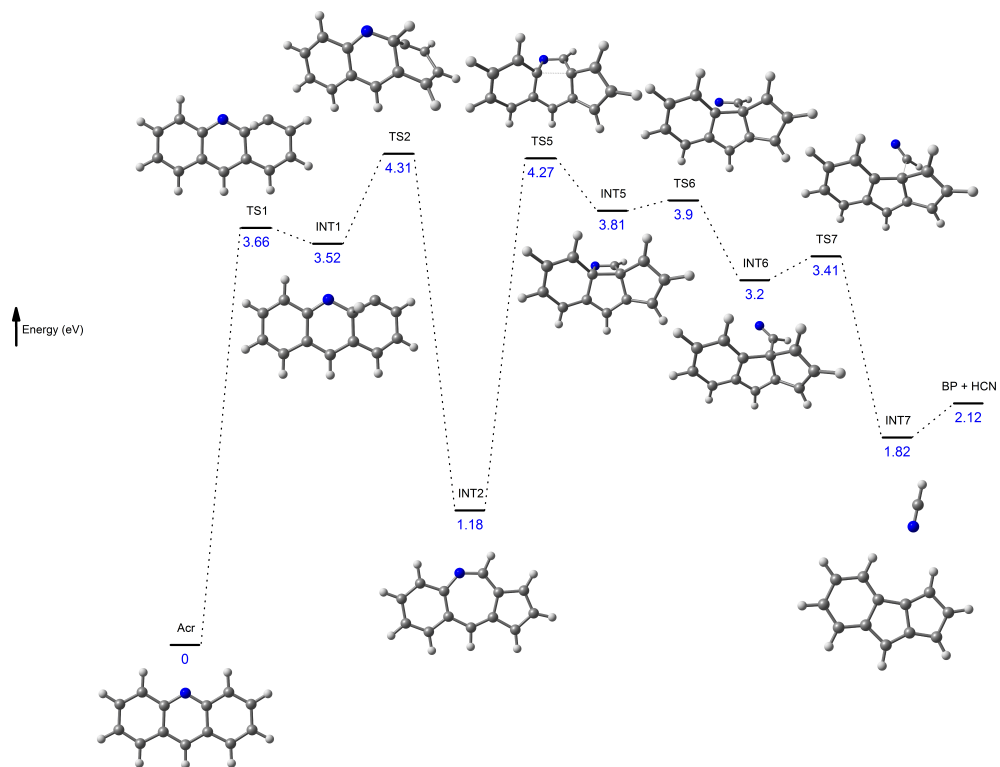


Figure 7: Potential energy surface leading from acridine⁺ to benzopentalene⁺.

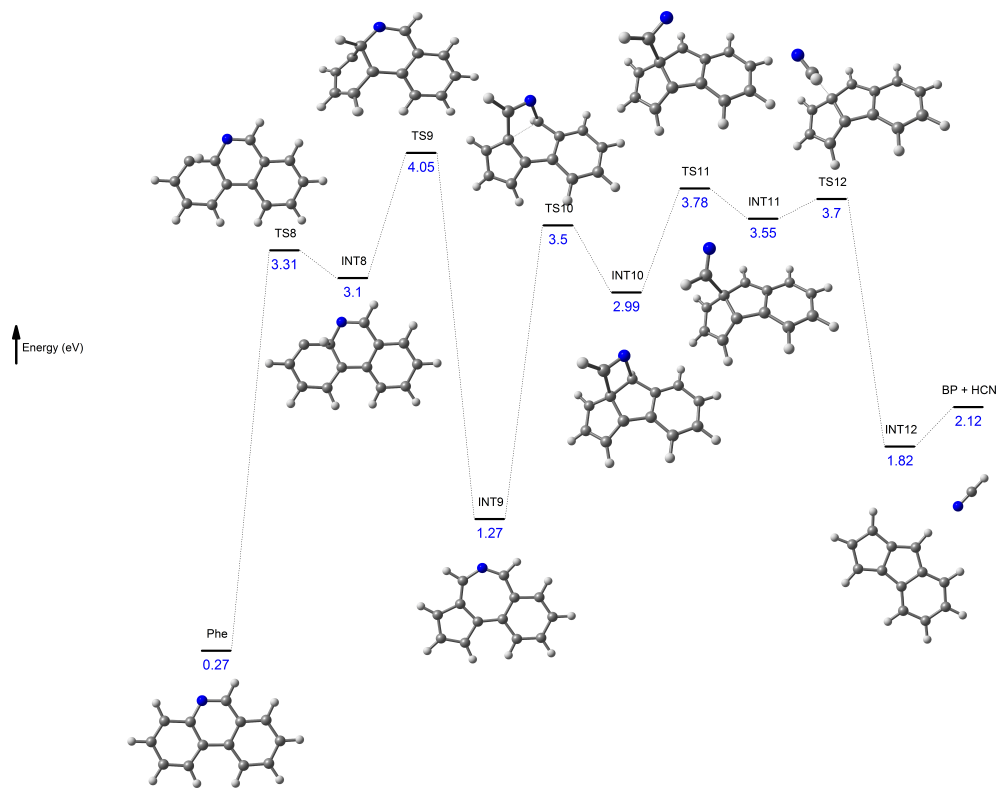


Figure 8: Potential energy surface leading from phenanthridine⁺ to benzopentalene⁺.

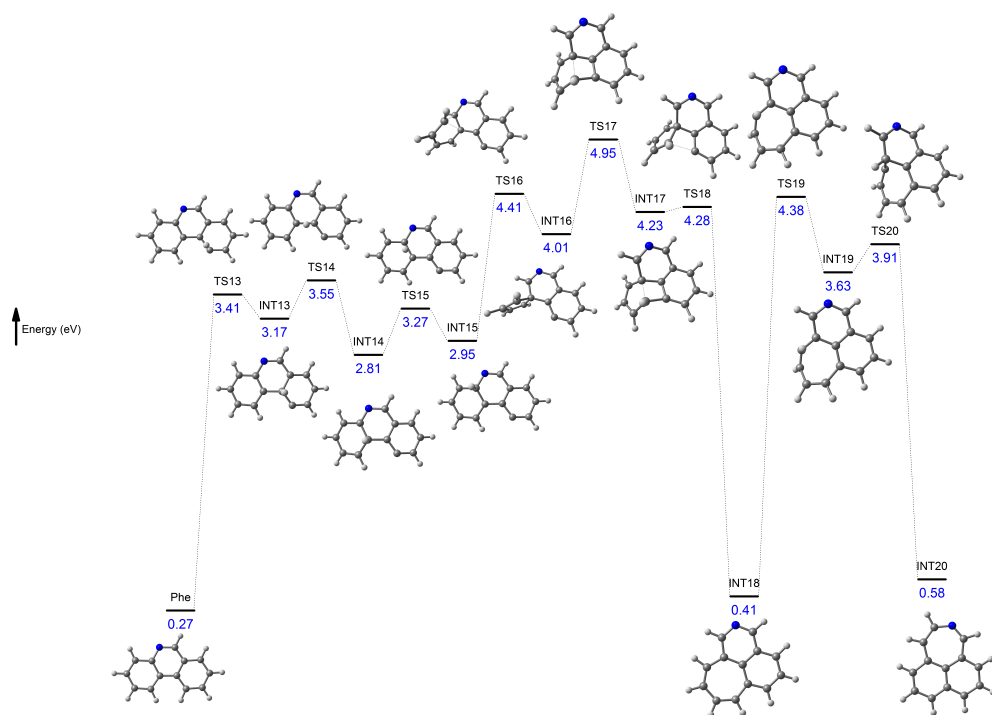


Figure 9: Potential energy surface leading from phenanthridine⁺ to INT20.

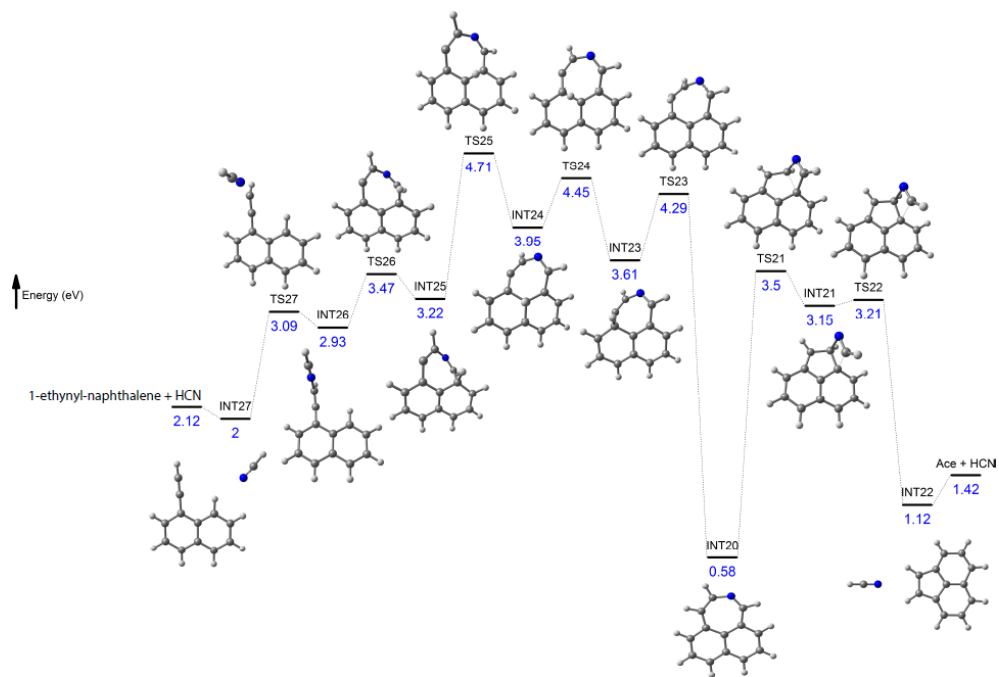


Figure 10: Potential energy surface leading from INT20 to 1-ethynyl-naphthalene⁺ and acenaphthylene⁺.

same common intermediate INT20. Figure 9 presents the steps leading from phenanthridine^{•+} to INT20. The pathway contains many intermediates and transition states including three hydrogen shifts. From INT20, expulsion of HCN from the central 7-membered ring leads to the formation of acenaphthylene over a rate-limiting transition state TS21 at 3.50 eV (Fig. 10). Alternatively, a series of hydrogen shifts (TS23 - TS27) are required to reach the 1-ethynynaphthalene product ion. The lowest energy paths from acridine^{•+} to AcN^{•+} and 1EN^{•+} also proceed via phenanthridine^{•+}.

References

- (1) Acheson, R. M.; Aplin, R. T.; Bolton, R. G. *Org. Mass Spectrom.* **1974**, *8*, 95–102.